AIAA AVIATION Forum
June 27-July 1, 2022, Chicago, IL & Virtual
AIAA AVIATION 2022 Forum

10.2514/6.2022-3889

3D Aircraft Control Surface Enabled by Co-Flow Jet Flap

Kewei Xu *, Gecheng Zha †
Dept. of Mechanical and Aerospace Engineering
University of Miami, Coral Gables, Florida 33124
E-mail: gzha@miami.edu

Abstract

This paper conducts Improved Delayed Detached Eddy Simulation to investigate the performance of a 3D aircraft control surface with Co-flow Jet (CFJ) active flow control applied on the flap with severe adverse pressure gradients (APG). For the numerical validation with the baseline control surfaces that have large flow separation, the predicted lift coefficient (C_L), drag coefficient (C_D), and pressure coefficient (C_p) distributions are in good agreement with the experiment at both deflection angle of 30° and 40°. The control surface using CFJ in the front main part with mild APG is also compared. With a small momentum coefficient (C_μ) of 0.025, the control surface using CFJ on the flap with severe APG outperforms the control surface using CFJ in the front main part in both control effectiveness and energy efficiency. Compared with the front CFJ control surface, the control surface with CFJ flap achieves 46.1% increase of lift coefficient with 80.8% lower power consumption. The improvement of the corrected aerodynamic efficiency $\Delta(C_L/C_D)_c$ is increased by 30.8%. The CFJ flap control surface also outperforms the Front CFJ configuration at the high deflection angle (δ) of 50° with C_L increased by 44.8% and $(C_L/C_D)_c$ increased by 6.8%. It can also attach the flow very well at δ of 70° and achieves a lift coefficient more than twice larger than the baseline. Overall, the CFJ flap control surface is more effective than the Front CFJ control surface to overcome adverse pressure gradients with attached flow using a smaller C_μ.

Nomenclature

AoA	Angle of attack
AFC	Active Flow Control
C	Chord length
CFJ	Co-flow jet
C_L	Lift coefficient
C_D	Drag coefficient
c_p	Constant pressure specific heat
C_p	Pressure coefficient, $(P - P_\infty)/(\frac{1}{2}\rho_\infty V_{\infty t}^2)$
C_μ	Jet momentum coefficient, $\dot{m}_j\, V_j/(\frac{1}{2}\rho_\infty V_\infty^2\, S)$
C_L/C_D	Aerodynamic efficiency
$(C_L/C_D)_c$	Aerodynamic efficiency corrected for CFJ airfoil

* Ph.D. Candidate
† Professor, AIAA associate Fellow

D	Total drag on the airfoil
$FASIP$	Flow-Acoustics-Structure Interaction Package
H_t	Total enthalpy
L	Total lift on the airfoil
LE	Leading Edge
$\dot{m}$	Mass flow rate
$\overline{\dot{m}}$	Non-dimensional mass flow rate, $\dot{m}/(V_\infty \rho_\infty S)$
M	Mach number
M_j	Injection Mach number
MAC	mean aerodynamic chord
P	CFJ Pumping power
P_c	Power coefficient, $P/(\frac{1}{2}\rho_\infty V_\infty^3 S)$
P_t	Total pressure
P_∞	Static pressure of free-stream
$RANS$	Reynolds-Averaged Navier-Stokes
R_e	Reynolds number
S	Planform area of the wing
TE	Trailing Edge
T_t	Total temperature
V_∞	Free-stream velocity
$V_{\infty t}$	Free-stream velocity normal to the wing LE, used to calculate C_p
V_j	Injection velocity
$ZNMF$	Zero-Net Mass Flux
c	Subscript, stands for corrected
j	Subscript, stands for jet
α	Angle of attack
β	Sideslip angle
γ	Air specific heats ratio
Γ	Total pressure ratio of CFJ pump
η	CFJ pumping system efficiency
ρ_∞	Free-stream density
δ	Deflection angle
θ_1	Angle between the injection slot surface and a line normal to the airfoil chord
θ_2	Angle between the suction slot surface and a line normal to the airfoil chord

1 Introduction

Aircraft control surfaces such as vertical tails, horizontal tails, and canards are responsible for maintaining aircraft stability. Control surfaces need to have high control authority by generating sufficient lift with rapid response time to keep the aircraft trimmed. To achieve such performance, control surfaces usually have large sizes, which bring severe penalties of weight, drag, and energy consumption.

Active Flow Control (AFC) as a mean to enhance lift has great potential to reduce the size and weight of control surfaces [1, 2, 3, 4, 5, 6, 7]. AFC is used to control the separated flow of vertical tails to enhance aerodynamic performance and mitigate flutter [8, 9, 10, 11, 12, 13, 14, 15, 16, 17]. The research

of Boeing and NASA [8, 9, 10, 11, 12, 13, 14, 15] on vertical tails using sweeping jets and synthetic jets AFC represents the state of the art. Rathay et.al [8] conducted wind tunnel experiments on a swept and tapered tail with a 29.6% chord rudder. Using flow control, the side force was increased by up to 18% at moderate rudder deflections with the AFC actuators operating at dimensionless frequency of O (10) [8] and a momentum coefficient C_μ=0.00721. Compared with synthetic jets, sweeping jets have higher C_μ output and corresponding jet velocity. Thus sweeping jets were selected over the synthetic jets by Boeing/NASA team for the subsequent full-scale AFC wind tunnel tests [9, 10].

The vertical tails with sweeping jets AFC were successfully tested on subscale models [11, 12], full-scale models [9, 10] and finally in flight [9]. The subscale test was performed at a 14% scaled model of Caltech and more than 50% of the side force enhancement was achieved by sweeping jet actuation with the momentum coefficient C_μ of 0.017. The full-scale vertical tail model equipped with sweeping jets AFC was tested at a nominal speed of 100 knots ($M_\infty \sim 0.15$, Re $\sim$ 15 million), a maximum speed of 130 knots ($M_\infty \sim 0.2$, Re $\sim$ 20 million), and across the vertical tail flight envelop for rudder deflections (0° to 30°) and sideslip angles (0° to −7.5°). A 31-actuator sweeping jets configuration produces significant flow attachment on the rudder, which results in 20% increase in side force for the maximum rudder deflection of 30° at the sideslip angle of 0° and -7.5°. Subsequently, the sweeping jets-enhanced vertical tail was flown on the Boeing 757 ecoDemonstrator in the spring of 2015. A side force increase of 13% to 16% was estimated at a 30° rudder deflection for the critical sideslip angle range between 0° and -7.5° with the sweeping jets. Kara [16, 17] analyzed the complex flow inside the sweeping jets for design optimization of actuator geometry with minimum pressure loss. However, the sweeping jets tend to suffer large energy loss due to the jet sweeping, 360° turning and massive flow separation. Furthermore, the system will also suffer an energy penalty due to introducing the air flow from engine bleed. The other challenging issue using engine bleed for flow control is that when the engines are idle at landing, they may not be able to provide sufficient mass flow.

Recently, Xu and Zha [18, 19] apply co-flow jet (CFJ) active flow control on the main part (front part before flap) of the 3D vertical tail control surface, which achieves substantial lift enhancement at low energy expenditure. Co-flow Jet (CFJ) airfoil [2, 5, 20, 21, 22, 23, 24, 25, 26, 27, 28] is a zero-net mass flux (ZNMF) flow control that does not need to use engine bleed. The advantage of applying CFJ on the front main part of a control surface is that the inner space is larger to facilitate embedding the CFJ actuators than the space of the flap. This is particularly true for small general aviation and unmanned aircraft. However, severe adverse pressure gradient (APG) and flow separation occur on the flap when it is deflected. The front part of a control surface has mild APG because it is aligned with the freestream flow. Our recent studies on the NASA hump [29, 30] indicate that applying CFJ in APG is more efficient and effective than in mild APG or favorable pressure gradient (FPG). This motivates the present study to apply the CFJ on the flap in severe APG. Compared with CFJ applied in the front part, applying CFJ on the flap is much more effective to increase the lift coefficient and requires a lower energy expenditure.

1.1 Co-Flow Jet

In the CFJ wing, an injection slot near leading edge (LE) and a suction slot near trailing edge (TE) on the wing suction surface are created as shown in Fig. 1. A small amount of mass flow is drawn into the wing near the TE, pressurized and energized by a micro-compressor pumping system inside the wing, and injected near the LE tangential to the main flow. The whole process does not add any mass flow to the system and hence is a ZNMF flow control.

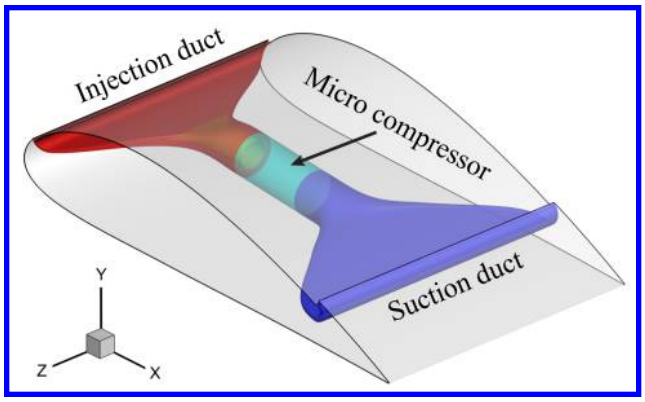

Figure 1: Schematics of the CFJ wing.

As described in [31, 32], a symmetric CFJ airfoil is used for the control surface as shown in Fig. 2. The injection slot and the suction slot are distributed on both sides of the CFJ control surface airfoil. When one side CFJ is working to generate side force, the other side CFJ is closed. The 3D CFJ control surface is created by extruding and tapering the 2D CFJ airfoil in a spanwise direction.

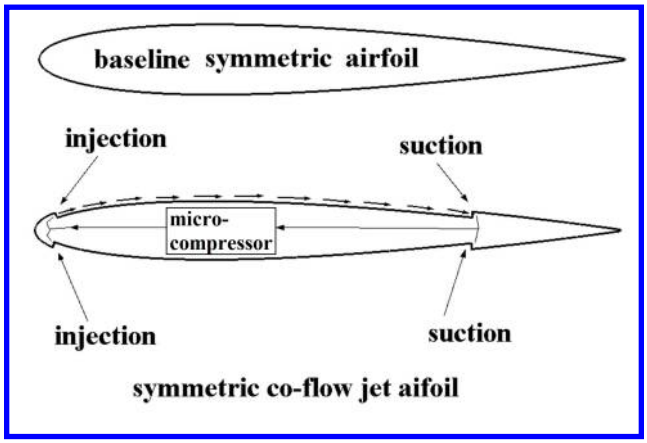

Figure 2: Schematics of the baseline and the CFJ control surface airfoils.

2 CFJ Parameters

This section lists the important parameters used to evaluate aerodynamic performance of a CFJ airfoil.

2.1 Jet Momentum Coefficient

The jet momentum coefficient C_μ is a parameter used to quantify the jet intensity. It is defined as:

$$C_\mu = \frac{\dot{m} V_j}{\frac{1}{2}\rho_\infty {V_\infty}^2 S} \tag{1}$$

where $\dot{m}$ is the injection mass flow, V_j is the mass-averaged injection velocity, ρ_∞ and V_∞ denote the free stream density and velocity, and S is the planform area.

2.2 Lift and Drag Calculation

For CFD simulation, the full reactionary forces produced by the momentum and pressure at the injection and suction slots are included by using control volume analysis. Zha et al.[20] gives the following formulations to calculate the lift and drag due to the jet reactionary force for a CFJ airfoil. By considering the effects of injection and suction jets on the CFJ airfoil, the expressions for these reactionary forces are given as :

$$F_{x_{cfj}} = (\dot{m}_j V_{j1} + p_{j1} A_{j1}) * cos(\theta_1 - \alpha) - (\dot{m}_j V_{j2} + p_{j2} A_{j2}) * cos(\theta_2 + \alpha) \tag{2}$$

$$F_{y_{cfj}} = (\dot{m}_{j1} V_{j1} + p_{j1} A_{j1}) * sin(\theta_1 - \alpha) + (\dot{m}_{j2} V_{j2} + p_{j2} A_{j2}) * sin(\theta_2 + \alpha) \tag{3}$$

where the subscripts 1 and 2 stand for the injection and suction respectively, and θ_1 and θ_2 are the angles between the injection and suction slot's surface and a line normal to the airfoil chord. α is the angle of attack.

The total lift and drag on the airfoil can then be expressed as:

$$D = R'_x - F_{x_{cfj}} \tag{4}$$

$$L = R'_y - F_{y_{cfj}} \tag{5}$$

where R'_x and R'_y are the surface integral of pressure and shear stress in x (drag) and y (lift) direction excluding the internal ducts of injection and suction. For CFJ wing simulations, the total lift and drag are calculated by integrating Eqs.(4) and (5) in the spanwise direction.

2.3 Power Coefficient

The power consumption is determined by the jet mass flow and total enthalpy change as the following:

$$P = \dot{m}(H_{t1} - H_{t2}) \tag{6}$$

where H_{t1} and H_{t2} are the mass-averaged total enthalpy in the injection cavity and suction cavity respectively, P is the power required by the pump and $\dot{m}$ the jet mass flow rate. Introducing P_{t1} and P_{t2} as the mass-averaged total pressure in the injection and suction cavity respectively, the pump efficiency η and the total pressure ratio of the pump $\Gamma = \frac{P_{t1}}{P_{t2}}$, the power consumption is expressed as:

$$P = \frac{\dot{m} c_p T_{t2}}{\eta} (\Gamma^{\frac{\gamma-1}{\gamma}} - 1) \tag{7}$$

where γ is the specific heat ratio equal to 1.4 for air, η is the micro-compressor efficiency with a typical value of 80% [28, 33], but in this paper, it is assumed as 100% to provide the required CFJ power. Eq. (7)

indicates that the power required for CFJ is linearly determined by the mass flow rate and exponentially by the total pressure ratio. This relationship in fact applies to all the active flow controls based on fluidic actuation. Thus, C_μ is not a suitable parameter to represent the power consumption of active flow control [5, 34, 35]. For example, a high C_μ could have a substantially lower power consumption than a lower C_μ if the large C_μ is created by a high mass flow rate and low jet velocity, which only needs a low total pressure ratio [5, 34, 35]. Since CFJ flow control is zero-net-mass-flux, all the mass flow is generated locally and a high mass flow or high C_μ is not a limitation for CFJ application. This is very different from the circulation control (CC) airfoil, for which the mass flow needs to be introduced from an external source (e.g., engine bleed).

The power coefficient is expressed as:

$$P_c = \frac{P}{\frac{1}{2}\rho_\infty V_\infty^3 S} \tag{8}$$

2.4 Corrected Aerodynamic Efficiency

The conventional wing aerodynamic efficiency is defined as:

$$\frac{C_L}{C_D} \tag{9}$$

For the CFJ wing, the ratio above still represents the pure aerodynamic relationship between lift and drag. However, since CFJ active flow control consumes energy, the ratio above is modified to take into account the energy consumption of the pump. The formulation of the corrected aerodynamic efficiency for CFJ wings is:

$$(\frac{C_L}{C_D})_c = \frac{C_L}{C_D + P_c} \tag{10}$$

where P_c is the power coefficient, L and D are the lift and drag generated by the CFJ wing. The formulation above converts the power consumed by the CFJ into a force $\frac{P}{V_\infty}$ which is added to the aerodynamic drag D. If the pumping power is set to 0, this formulation returns to the aerodynamic efficiency of a conventional wing.

3 Numerical Algorithms

The in-house high order accuracy CFD code Flow-Acoustics-Structure Interaction Package (FASIP) is used to conduct the numerical simulation. The 3D Improved Delayed Detached Eddy Simulation (IDDES) [36, 37, 38, 39] turbulence model is used. A 3rd order WENO scheme for the inviscid flux [40, 41, 42] and a 2nd order central differencing for the viscous terms are employed to discretize the Navier-Stokes equations. The low diffusion Roe scheme used as the approximate Riemann solver is utilized with the WENO scheme to evaluate the inviscid fluxes. Implicit time marching method using Gauss-Seidel line relaxation is used to achieve a fast convergence rate [43]. Parallel computing is implemented to save wall clock simulation time [44]. The FASIP code is intensively validated for various steady and unsteady 2D and 3D flows

including full aircraft [25, 45, 46], multi-stage compressors [47, 48, 49, 50, 49, 51], aero-elasticity flows [52, 53, 54, 55, 56, 57] and for CFJ 2D and 3D airfoil simulations [5, 20, 21, 22, 25, 26, 27, 39, 58, 59, 60]. Since the experimental results reported are time-averaged steady state results, the numerical results are also presented as the time-averaged results after the flow and all the aerodynamic forces become statistically stable.

4 Baseline Control Surface Validation

The baseline control surface model used in the present paper is adopted from the previous study [18], which is originally tested and simulated in [9, 10, 11, 12, 61]. The baseline vertical tail is tapered, swept with 42° and stacked using NACA0012 airfoil. The aspect ratio based on mean aerodynamic chord (MAC) is 1.98. Details of geometry are described in Ref. [18]. The free-stream conditions used in the present study are the same conditions as given by Seele et al in the experiment [12], which has the Reynolds number, Re_∞=1.36×10^6, incoming flow velocity, V_∞=40 m/s (about Mach 0.12), and sideslip angle β=0°. The front part of the control surface root is installed on the bottom wall. There is a small clearance between the flap and the wall resulting from flap deflection, and is simulated in this study as well as in the previous ones [18].

The computational domain is meshed using an O-type grid with a mesh size of 6.14 million cells (480 × 80 × 160). The results are stable after the characteristic time of 20 where the standard deviation (SD) of C_L and C_D for the last 200 time-step is in the order of 10^{-9} to 10^{-5}, and are virtually the machine zero compared with the C_L and C_D at order of 1. Details of mesh topology, boundary condition set-up and convergence history are presented in Ref. [18]. With the present mesh size, the predicted results achieve a good agreement with the experimental data with the C_L deviation of 3.8% and C_D deviation of 3.6% considering the massively separated flow due to the 30° deflected flap.

The computed results are further validated by examining the wing surface pressure coefficient distributions (C_p) at two deflection angles ($\delta = 30°$ and 40°). At each δ, two of three spanwise locations shown in Fig. 3 are selected for comparison, middle (70% span of at LE) and outboard (89% span of at LE). The inboard (40% span of LE) comparison is presented in Ref. [18]. As shown in Fig. 4, the pressure coefficient predicted by the present IDDES agrees well with the experimental data at δ= 30° and is slightly under estimated at δ= 40°, whereas the simulation of Vatsa et al [61] over-predicts the pressure on the pressure surface for both two span locations at two δ angles. Mesh refinement study is conducted by doubling the number of cells in i, j, k direction respectively as 960 × 80 × 160, 480 × 160 × 160 and 480 × 80 × 320. It is demonstrated in Ref. [18] that the numerical results of the baseline control surface are converged based on the initial mesh size of 6.14 million.

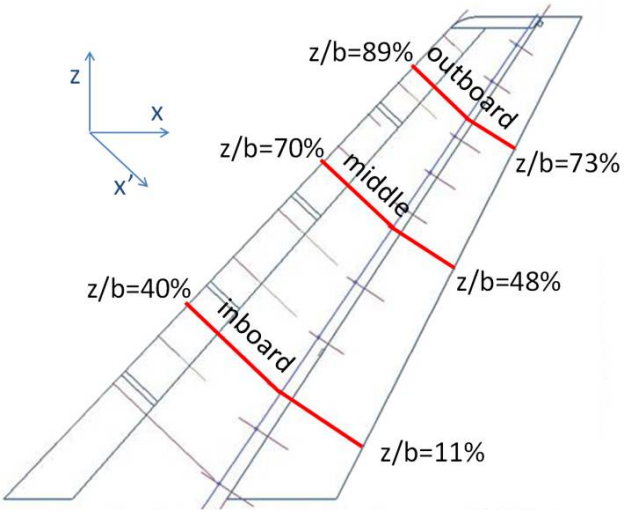

Figure 3: Illustration of span-wise pressure tap rows (picture adopted from [61]).

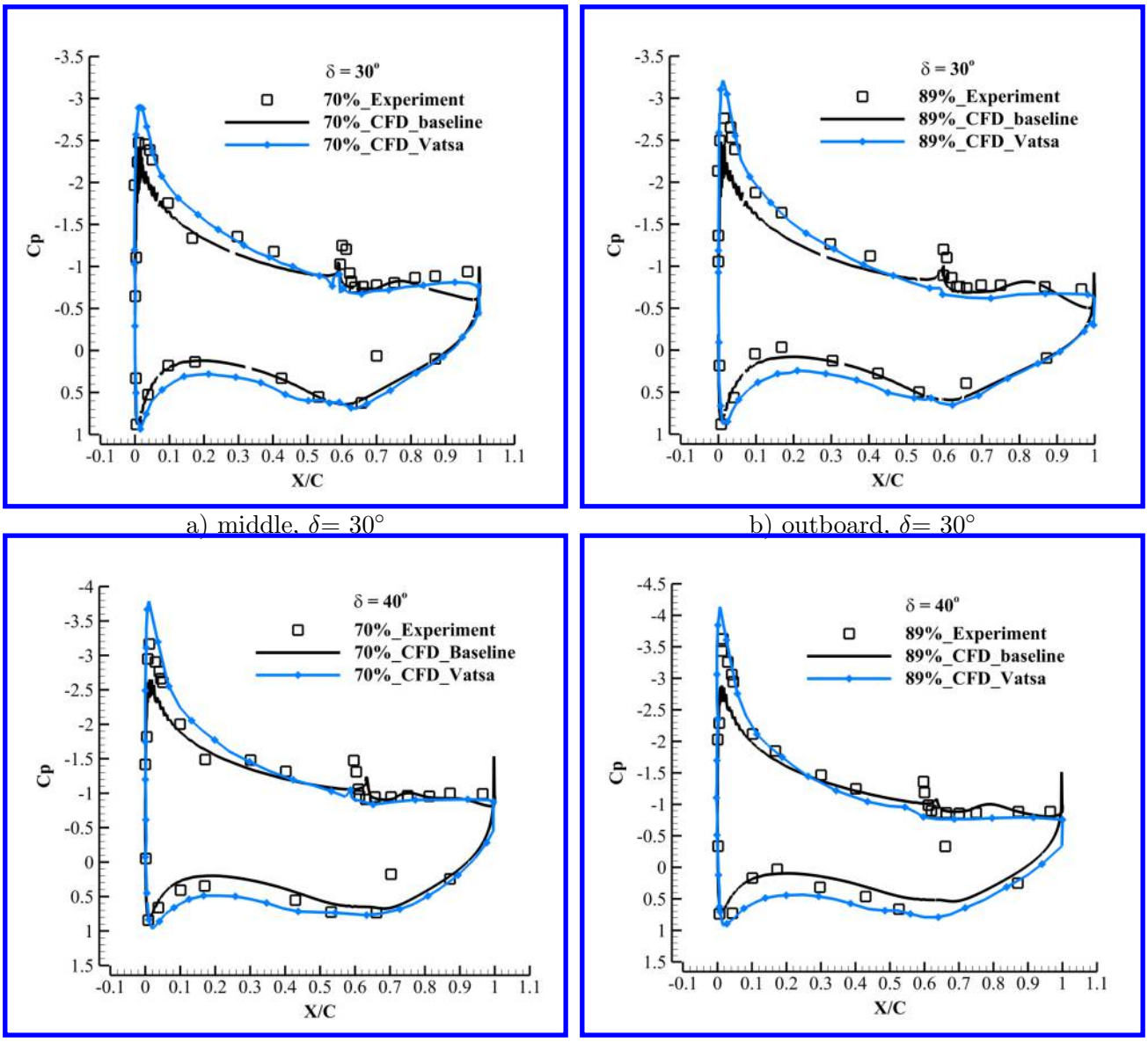

a) middle, δ= 30° b) outboard, δ= 30°

c) middle, δ= 40° d) outboard, δ= 40°

Figure 4: C_p comparisons of the baseline control surface at two deflection angles and two spanwise locations.

5 3D CFJ Control Surface

A 3D CFJ control surface is created based on the baseline configuration by adding an injection slot and suction slot. The previous study [18] has the CFJ applied on the front main part of the control surface as shown in Fig. 5 (a), which has the injection slot located at 4%C from the leading edge and the suction (blue) slot located at 63%C upstream of the flap. The mixing between CFJ and mainflow occurs in a mild adverse pressure gradient, which is named as Front CFJ. This paper studies a new configuration as shown in Fig. 5 (right) that the CFJ is applied on the flap with the injection located at 66%C from the leading edge and the suction is moved further downstream to 85%C. The new configuration is named Flap CFJ.

The injection slot size for the Flap CFJ control surface is 0.45%C and the suction slot size is 1%C.

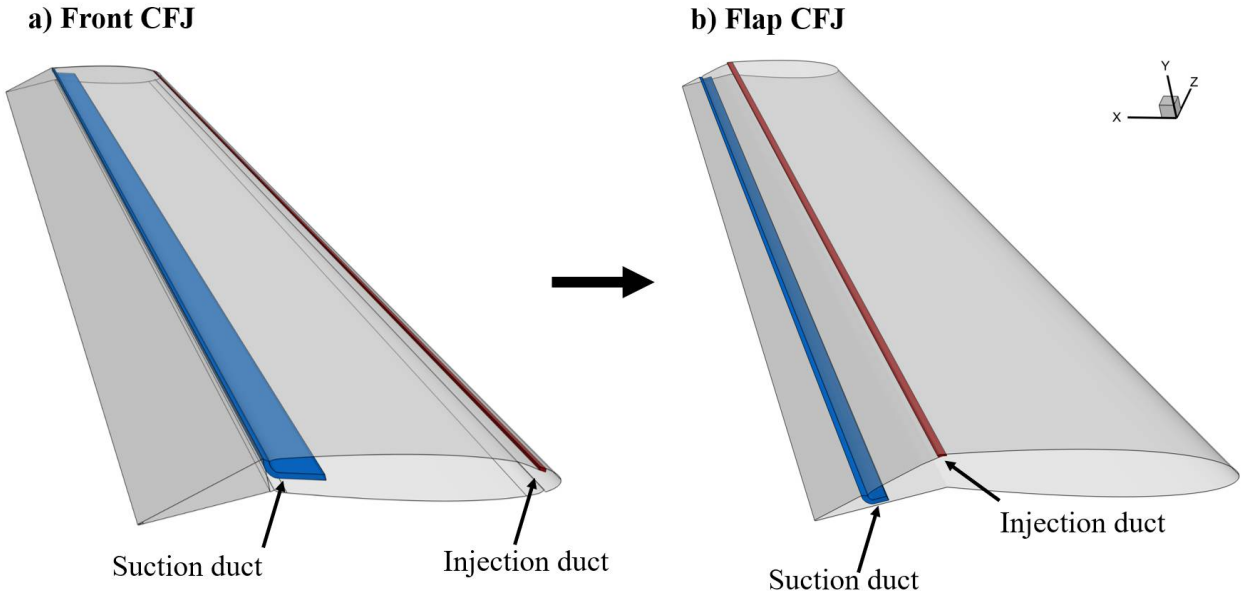

Figure 5: Geometry of the 3D CFJ control surfaces.

The mesh refinement study is also conducted for the control surface of Flap CFJ. The case showing the mesh refinement study herein has C_μ=0.025, β=0°, and δ=30°. The number of cells in i, j, k directions of CFJ are doubled respectively for the mesh refinement study. As presented in Table 1, the maximum variation of C_L, C_D and $(C_L/C_D)_c$ (defined in Eq. (10)) are 0.55%, 1.83% and 2.2%. Fig. 6 compares the C_p distributions calculated by the baseline mesh and refined mesh at two spanwise locations, which are virtually overlapped. These mesh refinement results demonstrate that the CFD solution is mesh independent.

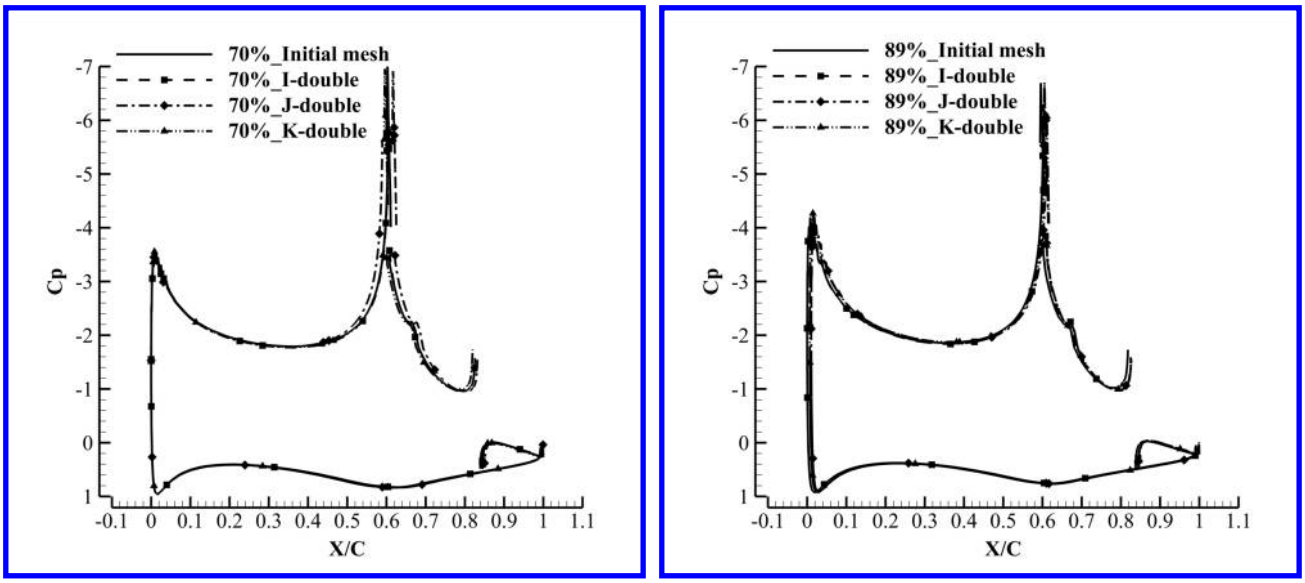

a) middle z/b = 70% b) outboard z/b = 89%

Figure 6: C_p distribution comparisons of the mesh refinement study of the Flap CFJ control surface at mid- and outer-span with C_μ=0.025, β=0°, and δ=30°.

Table 1: Mesh refinement studies of the Flap CFJ control surface with C_μ=0.025, β=0°, and δ=30°

Cases	Mesh size of CFJ	C_L	ΔC_L	C_D	ΔC_D	$(C_L/C_D)_c$	$\Delta(C_L/C_D)_c$
Baseline mesh	125 × 40 × 60	1.096	-	0.114	-	9.243	-
Doubled in i-direction	250 × 40 × 60	1.093	0.28%	0.114	0.40%	9.034	2.20%
Doubled in j-direction	125 × 80 × 60	1.093	0.26%	0.113	1.83%	9.382	1.50%
Doubled in k-direction	125 × 40 × 120	1.101	0.55%	0.115	1.30%	9.227	0.17%

5.1 Jet Momentum Coefficient (C_μ) Trade Study

The trade study with the jet momentum coefficients C_μ of 0.025, 0.05, 0.1, 0.2, and 0.26 is conducted to compare the aerodynamic performance for the Front CFJ and Flap CFJ control surfaces. The baseline control surface without CFJ is also presented as a reference. The sideslip angle (β) is fixed at 0° and the flap deflection angle (δ) is fixed at 30°. Table. 2 compares the aerodynamic performance of the baseline, Front CFJ at C_μ=0.025 and Flap CFJ cases at various C_μ. Compared with the baseline control surface, both the Front and Flap CFJ cases largely increase the lift coefficient C_L by 28.1% and 46.1% respectively at C_μ of 0.025. Clearly, the Flap CFJ is much more effective to increase the lift coefficient. Furthermore, the power coefficient of the Flap CFJ is 81% smaller than the Front CFJ case. This results in an increase of $(C_L/C_D)_C$ by 32.8% and 30.3% respectively compared with that of the baseline and Front CFJ configuration. In other words, the CFJ control surface with CFJ applied at the front or flap is able to achieve a significant control effectiveness while maintaining a high energy efficiency.

Table 2: Aerodynamic performance of the control surface with different C_μ

Cases	C_μ	C_L	ΔC_L	C_D	P_c	C_L/C_D	$(C_L/C_D)_c$	$\Delta(C_L/C_D)_c$	Γ
Baseline EXP [61]		0.78	-	0.112	-	6.96	6.96	-	-
Baseline CFD	-	0.75	-	0.108	-	6.93	6.93	-	-
Front CFJ	0.025	0.96	28.1%	0.109	0.026	8.84	7.09	2.3%	1.02
Flap CFJ	0.025	1.095	46.1%	0.113	0.005	9.65	9.24	33.1%	1.006
Flap CFJ	0.05	1.166	55.5%	0.115	0.017	10.16	8.85	27.5%	1.013
Flap CFJ	0.1	1.234	64.5%	0.104	0.054	11.89	7.79	12.1%	1.030
Flap CFJ	0.2	1.323	76.4%	0.076	0.217	17.35	4.51	-35.0%	1.083
Flap CFJ	0.26	1.365	82.0%	0.056	0.461	24.36	2.64	-62.0%	1.154

Fig. 7 compares the aerodynamic performance between the Front and Flap CFJ at various C_μ with the data of Front CFJ adopted from our previous work [18]. Baseline case is shown in the blue line as a reference. As shown in Fig. 7 (a), at the small C_μ regime below 0.05, the lift coefficient of the Flap CFJ control surface is higher than the FPG injection, whereas the Front CFJ performs better at the high C_μ regime. This is because applying CFJ at flap, the adverse pressure gradient (APG) region is more efficient and effective to remove flow separation [29, 30]. In other words, APG injection achieves a better attachment with a smaller C_μ. In fact, at the small C_μ of 0.025 and 0.05, the Flap CFJ achieves a higher improvement of lift (ΔC_L) and corrected aerodynamic efficiency $\Delta(C_L/C_D)_c$ simultaneously, as compared to the Front CFJ. Fig. 7 (b) shows that both CFJ configurations have C_D reduced with the increasing of C_μ. The power coefficient increases significantly with the C_μ increase as shown in Fig. 7 (d). This is because P_c is exponentially determined by the total pressure ratio (Γ, Fig. 7 (f)) of CFJ micro-compressor actuator. A high Γ therefore leads to a much higher P_c. The flap CFJ has a lower P_c in all C_μ and as a result, its $(C_L/C_D)_c$ is boosted as illustrated in Fig. 7 (e).

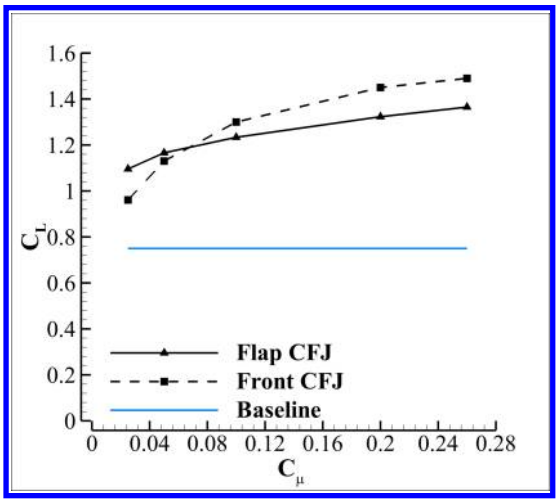

a) Lift coefficient (C_L)

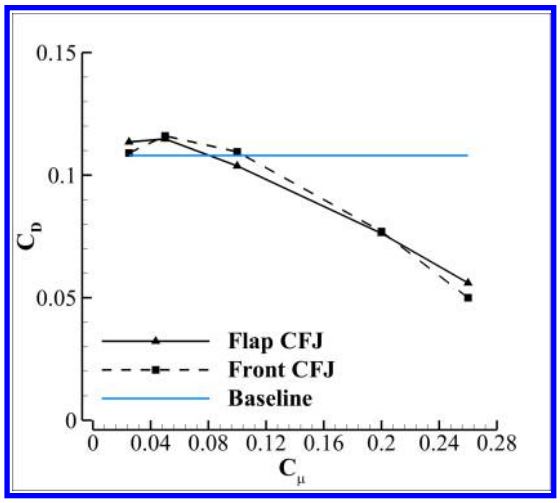

b) Drag coefficient (C_D)

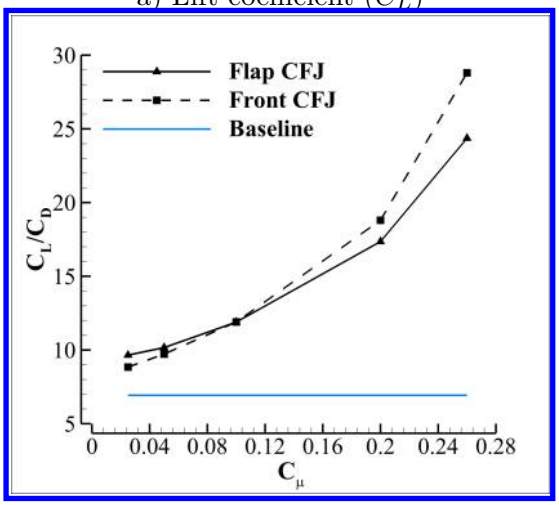

c) Aerodynamic efficiency (C_L/C_D)

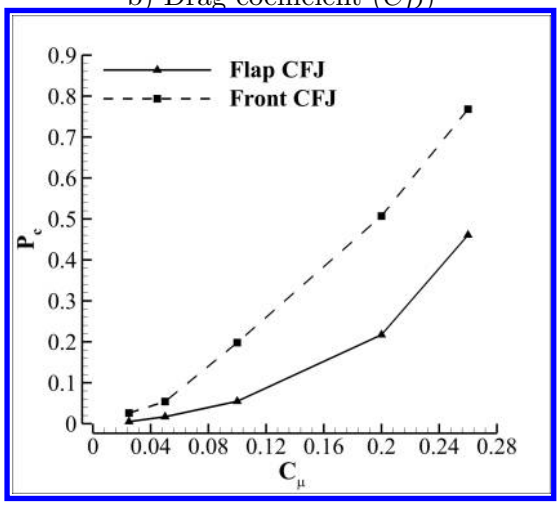

d) Power coefficient (P_e)

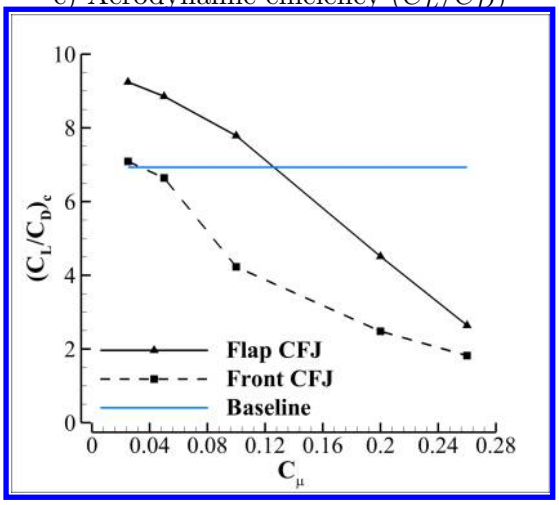

e) Corrected aerodynamic efficiency ($(C_L/C_D)_c$)

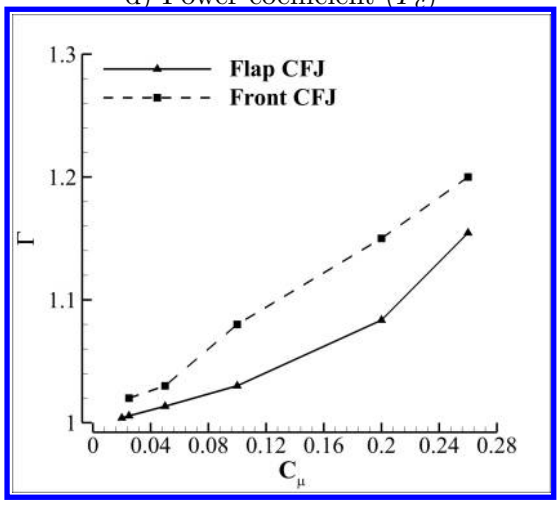

f) Total pressure ratio of CFJ (Γ)

Figure 7: Comparison of aerodynamic performance between Flap and Front CFJ control surface with various C_μ, β=0°, and δ=30°.

Since the Flap CFJ achieves both high effectiveness and efficiency at C_μ=0.025, its flow-field compared with the Baseline and Front CFJ illustrated by Mach-number-colored streamlines is shown in Fig. 8. Severe flow separation is observed at the flap region of the baseline control surface as shown in Fig. 8 (a). With CFJ applied in the front region in Fig. 8 (b), flow separation at the flap region is largely suppressed but spanwise flow migration can be still clearly seen. The Flap CFJ has streamlines well aligned in the streamwise direction with much less spanwise flow migration, which also mitigates the tip vortex. This is because applying CFJ near separation onset location where the flap starts to deflect is the most effective to suppress flow separation [29, 30]. Such high control effectiveness is also evidenced by C_p distributions in Fig. 9. At both middle and outboard span-locations, the Flap CFJ achieves a much lower pressure on the suction surface at the flap region (X/C = 0.63 - 1.0).

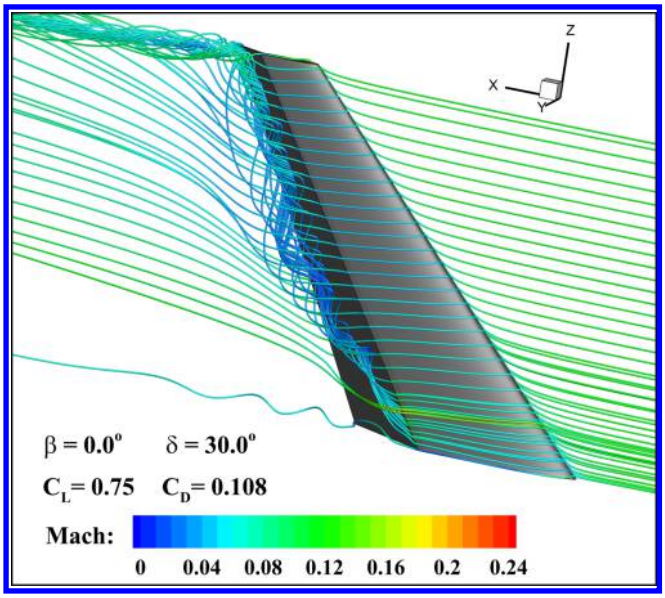

a) Baseline

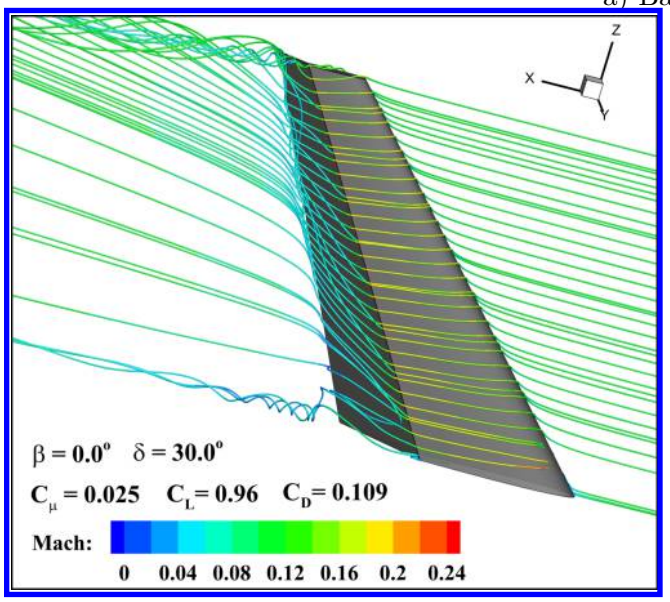

b) Front CFJ

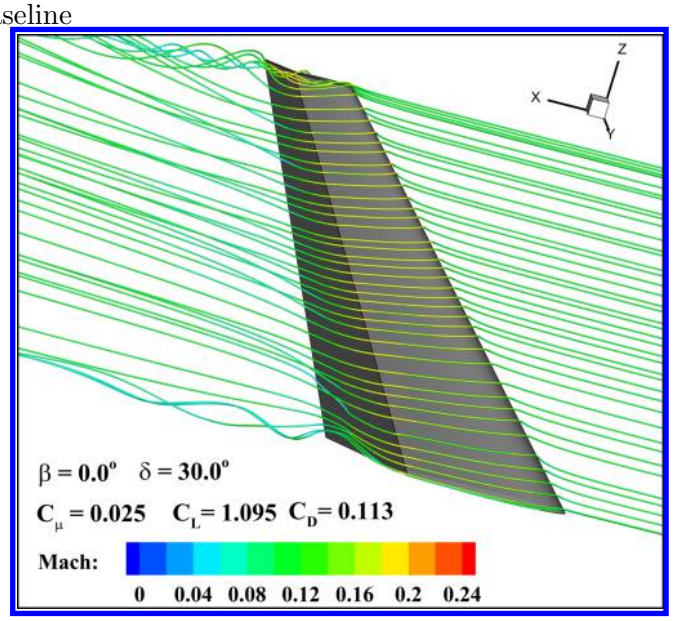

c) Flap CFJ

Figure 8: Streamlines of the baseline and CFJ control surfaces

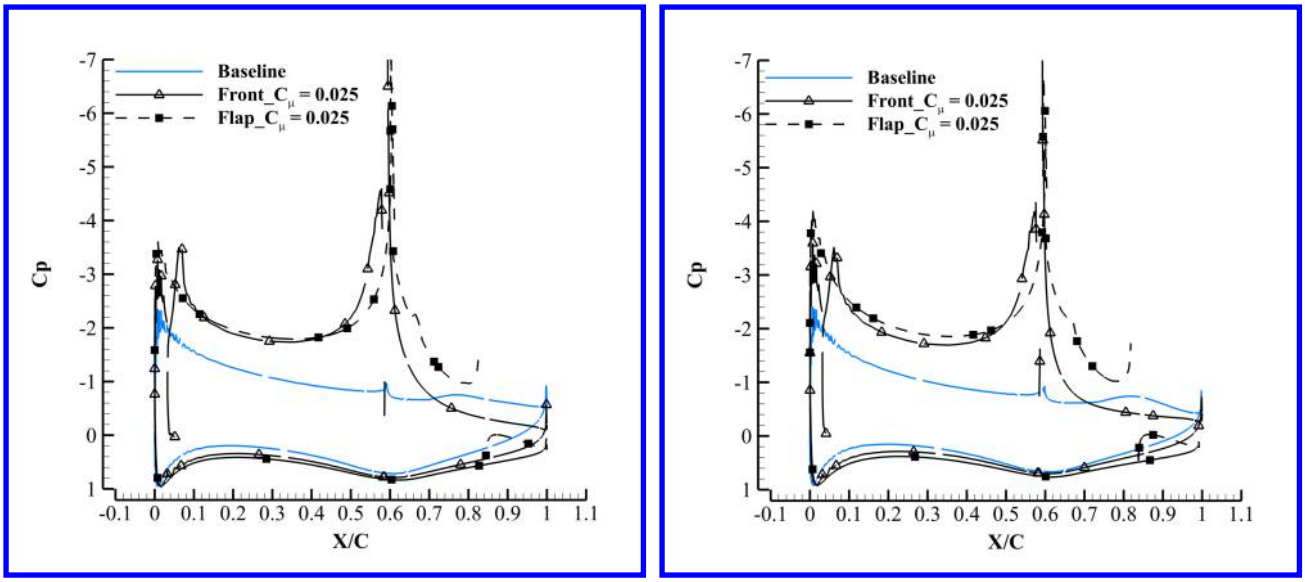

a) middle at z/b = 70% b) outboard at z/b = 89%

Figure 9: C_p distribution comparisons of Front and Flap CFJ control surface at mid- and outer-span with C_μ=0.025, β=0°, and δ=30°.

5.2 Deflection angle (δ) Variation

This section studies the effects of the deflection angle (δ) variation on the performance of the Flap CFJ control surface. Results are presented with two C_μ of 0.05 and 0.2 representing the low and high jet intensity respectively. Four deflection angles of 30°, 40°, 50°, and 70° are studied for the Flap CFJ control surface, the Front CFJ configuration only has the results presented for the deflection angle of 30, 40 and 50, which were simulated in the previous study [18] and are used here for comparison.

Fig. 10 plots the C_L, C_D, P_c, and $(C_L/C_D)_c$ varying with δ angles for the Flap CFJ (solid line) and Front CFJ (dashed line) with C_μ of 0.05 (hollow symbols) and 0.2 (solid symbols). The performance of the baseline control surface is plotted by the blue lines where its $(C_L/C_D)_c$ is plotted in Fig. 10 (d) instead of (C_L/C_D). With a small C_μ=0.05, Flap CFJ achieves a higher C_L than the Front CFJ in all δ angles due to the effective control of the flow separation at the flap region. The control effectiveness of the Front CFJ at the small C_μ is weakening towards the high δ because the flow separation is too severe to control at the high defection angle. Comparatively, solid lift enhancements are still achieved in the Flap CFJ, even at δ=70°. With a high C_μ of 0.2 applied, the Front CFJ has a higher C_L at the low δ of 30° and 40° but is outperformed at a higher δ angle, which is again due to the strong flow separation at the flap. For the drag coefficient shown in Fig. 10 (b), both configurations behave similarly that have an increasing drag with the increase of δ angle. On the one hand, this is because pressure drag increases as the flap deflects more. On the other hand, as the flow separation is removed with a better attachment on the flap, flow accelerates at the deflection due to the high turning, which reduces the pressure on the suction side and contributes to drag increase. It is also noteworthy that the low C_μ help reduce drag at a low deflection angle of 30° as compared to the baseline case. This is because the pressure increased by the removal of flow separation outweighs the pressure reduction from the jet attachment on the deflection region. Such drag reduction can be only achieved in low deflection angle cases. The power coefficient (P_c) varying with different δ is shown in Fig. 10 (c). The Flap CFJ has a much lower P_c at low δ angle conditions, about

1/3 of the Front CFJ with C_μ=0.05 and δ=30°. Such low P_c contributes to the high $(C_L/C_D)_c$ as shown in Fig. 10 (d). Overall, the Flap CFJ is more effective to overcome adverse pressure gradients, which can remove flow separation with smaller C_μ than the Front CFJ. Therefore, the control using Flap CFJ has both high effectiveness and efficiency. However, once flow attachment is achieved, further increasing C_μ brings minor improvements compared to the Front CFJ.

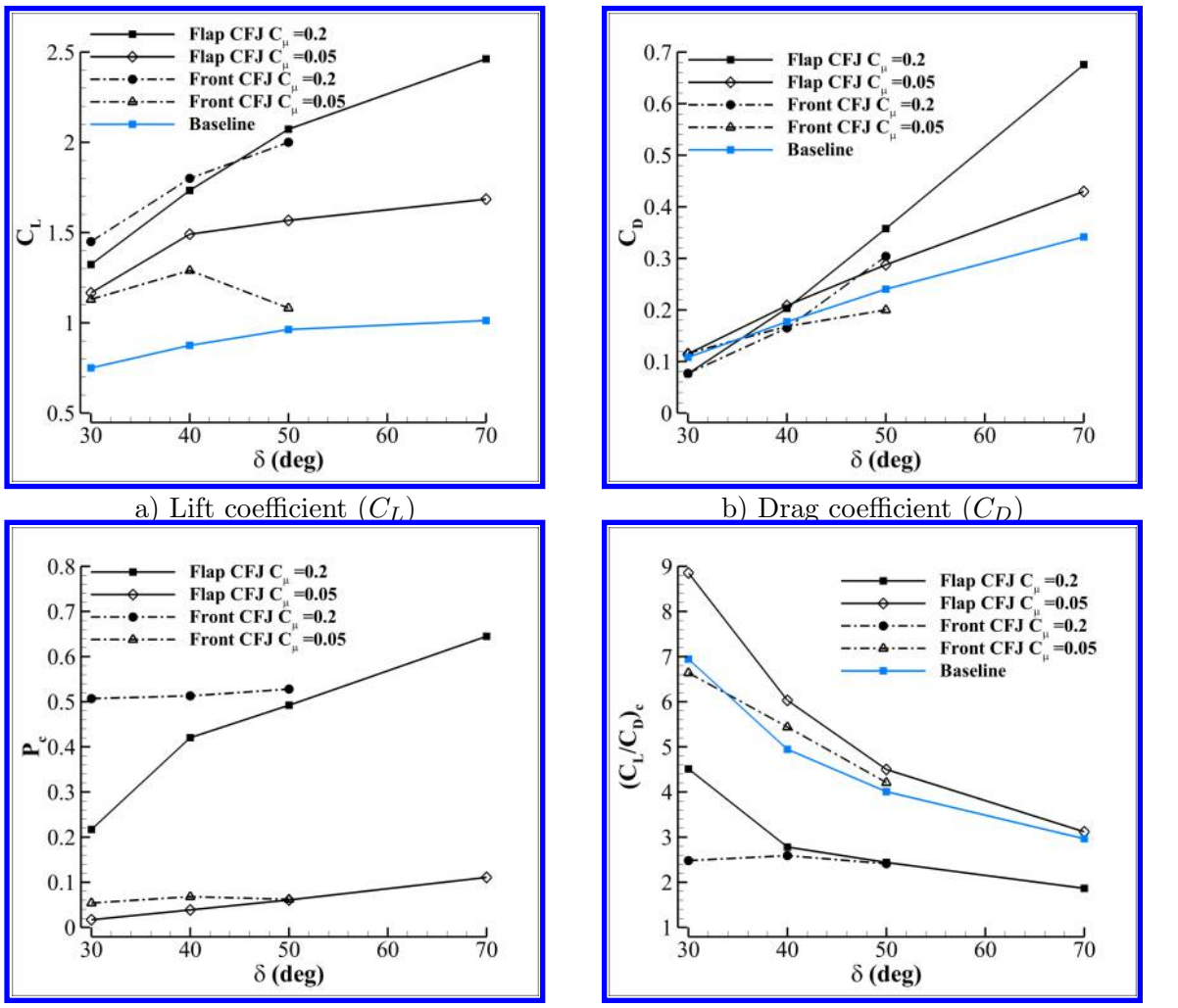

a) Lift coefficient (C_L) b) Drag coefficient (C_D)

c) Power coefficient (P_c) d) Corrected aerodynamic efficiency ($(C_L/C_D)_c$)

Figure 10: Comparison of aerodynamic performance between Flap and Front CFJ control surface with various δ, and C_μ of 0.05 and 0.2.

Fig. 11 shows the streamlines (colored by Mach number) of the Flap CFJ control surfaces at four deflection angles with C_μ=0.2. The flow in all cases is well attached along the major span except the near tip and root regions. Flow accelerates at the locations that the flap deflects and the acceleration is enhanced with the increasing δ angle due to the attached flows with a higher turning. The observed root vortex is caused by the gap between the deflected flap and the wall, which is intensified as the gap increases towards the high deflection angles. The tip vortex becomes very strong at δ angle of 70° due to the enhanced pressure difference between the pressure and suction sides of the flap. However, the flow is still very well attached and aligned with the streamwise direction in the majority of the span. The lift

coefficient (C_L) at this condition is 2.46, a 125% increase compared with the baseline control surface. In principle, a CFJ control surface with 44% of the baseline control surface (C_L=1.09) can achieve the same side force, which would bring a substantial weight and drag reduction to the whole aircraft system.

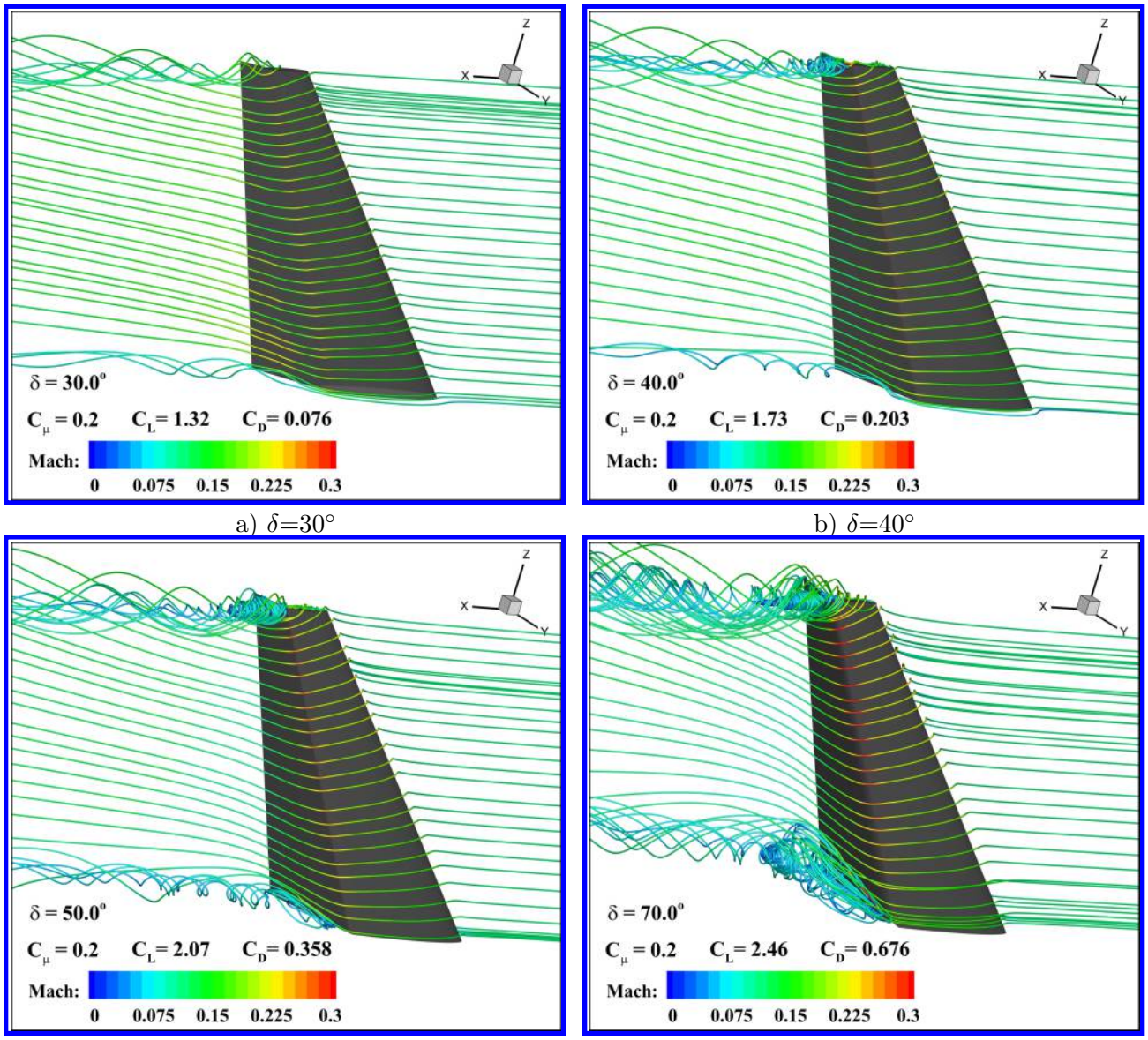

a) δ=30° b) δ=40°

c) δ=50° δ=70°

Figure 11: Streamlines of Flap CFJ cases with various δ and C_μ of 0.2.

6 Conclusion

Improved Delayed Detached Eddy Simulation is conducted to investigate the performance of a 3D aircraft control surface with Co-flow Jet (CFJ) active flow control applied on the flap with severe adverse pressure gradients (APG). The control surface using CFJ in the front main part with mild APG is also presented for comparison. With a small momentum coefficient (C_μ) of 0.025, the control surface using CFJ on the

flap with severe APG outperforms the control surface using CFJ in the front main part in both control effectiveness and energy efficiency. The control surface with CFJ flap achieves 46.1% increase of lift coefficient with 80.8% lower power consumption than the Front CFJ configuration. The improvement of the corrected aerodynamic efficiency $\Delta(C_L/C_D)_c$ is increased by 30.8%. The CFJ flap control surface also outperforms the Front CFJ at the high deflection angle (δ) of 50° with C_L increased by 44.8% and $(C_L/C_D)_c$ increased by 6.8%. It can also attach the flow very well at δ of 70° and achieves a lift coefficient more than twice larger than the baseline. Overall, the CFJ flap control surface is more effective than the Front CFJ control surface to overcome adverse pressure gradients with attached flow using a smaller C_μ.

7 Acknowledgment

The authors would like to acknowledge the computing resource provided by the Center for Computational Sciences at the University of Miami.

Disclosure: The University of Miami and Dr. Gecheng Zha may receive royalties for future commercialization of the intellectual property used in this study.

References

[1] S. Anders, W. Sellers III, and A. Washburn, "Active flow control activities at nasa langley." AIAA Paper 2004-2623, 2nd AIAA Flow Control Conference, Portland, Oregon, DOI: 10.2514/6.2004-2623, 28 June 2004 - 01 July 2004.

[2] G.-C. Zha, B. F Carroll, C. D. Paxton, C. A. Conley, and A. Wells, "High-performance airfoil using coflow jet flow control," *AIAA journal*, vol. 45, no. 8, pp. 2087–2090, 2007, DOI: 10.2514/1.20926.

[3] W. Bower and V. Kibens, "An overview of active flow control applications at the boeing company." AIAA Paper 2004-2624, 2nd AIAA Flow Control Conference, Portland, Oregon, 28 June 2004 - 01 July 2004, DOI: 10.2514/6.2004-2624.

[4] O. Kandil, E. Gercek, X. Zheng, and X. Luo, "Development of computational sensing and active flow control of airfoils during dynamic stall," in *42nd AIAA Aerospace Sciences Meeting and Exhibit*, AIAA 2004-0043, DOI: 10.2514/6.2004-43.

[5] A. Lefebvre, B. Dano, W. Bartow, M. Fronzo, and G. Zha, "Performance and energy expenditure of coflow jet airfoil with variation of Mach number," *Journal of Aircraft*, vol. 53, no. 6, pp. 1757–1767, 2016, DOI: 10.2514/1.C033113.

[6] T. Van Buren and M. Amitay, "Comparison between finite-span steady and synthetic jets issued into a quiescent fluid," *Experimental Thermal and Fluid Science*, vol. 75, pp. 16–24, 2016, DOI: 10.1016/j.expthermflusci.2016.01.014.

[7] L. Pack, N. Schaeffler, C. Yao, and A. Seifert, "Active control of flow separation from the slat shoulder of a supercritical airfoil." AIAA Paper 2002-3156, 1st Flow Control Conference, St. Louis, Missouri, 24 June 2002 - 26 June 2002, DOI: 10.2514/6.2002-3156.

[8] N. W. Rathay, M. J. Boucher, M. Amitay, and E. Whalen, "Performance enhancement of a vertical tail using synthetic jet actuators," *AIAA Journal*, vol. 52, no. 4, pp. 810–820, 2014, DOI: 10.2514/1.J052645.

[9] J. C. Lin, M. Y. Andino, M. G. Alexander, E. A. Whalen, M. A. Spoor, J. T. Tran, and I. J. Wygnanski, "An overview of active flow control enhanced vertical tail technology development." AIAA Paper 2016-0056, 54th AIAA Aerospace Sciences Meeting, San Diego, California, USA, 4-8 January 2016, DOI: 10.2514/6.2016-0056.

[10] M. Y. Andino, J. C. Lin, A. E. Washburn, E. A. Whalen, E. C. Graff, and I. J. Wygnanski, "Flow separation control on a full-scale vertical tail model using sweeping jet actuators." AIAA Paper 2015-0785, 53rd AIAA Aerospace Sciences Meeting, Kissimmee, Florida, 5-9 January 2015, DOI: 10.2514/6.2015-0785.

[11] R. Seele, E. Graff, M. Gharib, L. Taubert, J. Lin, and I. Wygnanski, "Improving rudder effectiveness with sweeping jet actuators." AIAA Paper 2012-3244, 6th AIAA Flow Control Conference, New Orleans, Louisiana, 25 June 2012 - 28 June 2012, DOI: 10.2514/6.2012-3244.

[12] R. Seele, E. Graff, J. Lin, and I. Wygnanski, "Performance enhancement of a vertical tail model with sweeping jet actuators." AIAA Paper 2013-0411, 51st AIAA Aerospace Sciences Meeting including the New Horizons Forum and Aerospace Exposition, Grapevine (Dallas/Ft. Worth Region), Texas, 07 January 2013 - 10 January 2013, DOI: 10.2514/6.2013-411.

[13] N. Rathay, M. Boucher, M. Amitay, and E. Whalen, "Parametric study of synthetic-jet-based control for performance enhancement of a vertical tail," *AIAA Journal*, vol. 52, no. 11, pp. 2440–2454, 2014, DOI: 10.2514/1.J052887.

[14] E. Graff, R. Seele, J. C. Lin, and I. Wygnanski, "Sweeping jet actuators-a new design tool for high lift generation." 20130013994, Innovative Control Effectors for Military Vehicles (AVT-215), Stockholm, Sweden, 20-22 May 2013.

[15] A. Shmilovich, Y. Yadlin, and E. Whalen, "Computational evaluation of flow control for enhanced control authority of a vertical tail," *AIAA Journal*, vol. 45, no. 8, pp. 2211–2220, 2016, DOI: 10.2514/1.J054712.

[16] K. Kara, "Numerical simulation of a sweeping jet actuator." AIAA Paper 2016-3261, 34th AIAA Applied Aerodynamics Conference, Washington, D.C., 13-17 June 2016, DOI: 10.2514/6.2016-3261.

[17] K. Kara, "Numerical study of internal flow structures in a sweeping jet actuator." AIAA Paper 2015-2424, 33rd AIAA Applied Aerodynamics Conference,Dallas, TX, 22-26 June 2015, DOI: 10.2514/6.2015-2424.

[18] Xu, K. and Zha, G.-C., "High Control Authority 3D Aircraft Control Surfaces Using Co-Flow Jet." AIAA Journal of Aircraft (2020), July 14, 2020. DOI: 10.2514/1.C035727, 2020.

[19] K. Xu and G. Zha, "High control authority 3d aircraft control surfaces using co-flow jet," in *AIAA Aviation 2019 Forum*, pp. AIAA Paper 2019–3168, 17-21 June 2019, Dallas, Texas, DOI: 10.2514/6.2019-3168.

[20] G. Zha, W. Gao, and C.D. Paxton, "Jet Effects on Co-Flow Jet Airfoil Performance," *AIAA Journal*, vol. 45, pp. 1222–1231, DOI: 10.2514/1.23995, 2007.

[21] G.-C. Zha, C. Paxton, A. Conley, A. Wells, nd B. Carroll, "Effect of Injection Slot Size on High Performance Co-Flow Jet Airfoil," *AIAA Journal of Aircraft*, vol. 43, pp. 987–995, DOI: 10.2514/1.16999, 2006.

[22] B. Wang, B. Haddoukessouni, J. Levy, and G.-C. Zha, "Numerical investigations of injection-slot-size effect on the performance of coflow jet airfoils," *Journal of Aircraft*, vol. 45, no. 6, pp. 2084–2091, 2008, DOI: 10.2514/1.37441.

[23] B. P. E. Dano, D. Kirk, and G.-C. Zha, "Experimental Investigation of Jet Mixing Mechanism of Co-Flow Jet Airfoil." AIAA-2010-4421, 5th AIAA Flow Control Conference, Chicago, IL, 28 Jun - 1 Jul 2010, DOI: 10.2514/6.2010-4421.

[24] B. Dano, G. Zha, and M. Castillo, "Experimental study of co-flow jet airfoil performance enhancement using discreet jets." AIAA Paper 2011-941, 49th AIAA Aerospace Sciences Meeting including the New Horizons Forum and Aerospace Exposition, Orlando, Florida, 04 January 2011 - 07 January 2011, DOI: 10.2514/6.2011-941.

[25] Lefebvre, A. and Zha, G.-C. , "Design of High Wing Loading Compact Electric Airplane Utilizing Co-Flow Jet Flow Control." AIAA Paper 2015-0772, AIAA SciTech2015: 53nd Aerospace Sciences Meeting, Kissimmee, FL, 5-9 Jan 2015, DOI: 10.2514/6.2015-0772.

[26] Liu, Z.-X. and Zha, G.-C., "Transonic Airfoil Performance Enhancement Using Co-Flow Jet Active Flow Control." AIAA Paper 2016-3066, AIAA Aviation, Washington, D.C., June 13-17 2016, DOI: 10.2514/6.2016-3472.

[27] Lefebvre, A. and Zha, G.-C., "Trade Study of 3D Co-Flow Jet Wing for Cruise and Takeoff/Landing Performance." AIAA Paper 2016-0570, AIAA SCITECH2016, AIAA Aerospace Science Meeting, San Diego, CA, 4-8 January 2016, DOI: 10.2514/6.2016-0570.

[28] G. Zha, Y. Yang, Y. Ren, and B. McBreen, "Super-lift and thrusting airfoil of coflow jet actuated by micro-compressors," in *2018 Flow Control Conference, Atlanta, Georgia, June 25-29*, AIAA 2018-3061, 2018, DOI: 10.2514/6.2018-3061.

[29] K. Xu, Y. Ren, and G.-C. Zha, "Numerical analysis of energy expenditure for co-flow wall jet separation control," *AIAA 2022 SciTech Forum*, 2022.

[30] Xu, K. and Ren, Y. and Zha, G.-C., "Separation Control by Co-Flow Wall Jet," in *AIAA 2021 Aviation Forum, AIAA 2021-2946*, Virtual Event, June 2021, DOI: 10.2514/6.2021-2946.

[31] J. Zhang, K. Xu, Y. Yang, Y. Ren, P. Patel, and G. Zha, "Aircraft control surfaces using co-flow jet active flow control airfoil." AIAA Paper 2018-3067, 2018 Applied Aerodynamics Conference, Atlanta, Georgia, June 25-29, 2018, DOI: 10.2514/6.2018-3067.

[32] K. Xu, J. Zhang, and G. Zha, "Drag minimization of co-flow jet control surfaces at cruise conditions." AIAA 2019-1848, AIAA Scitech 2019 Forum, San Diego, California, 7-11 January 2019, DOI: 10.2514/6.2019-1848.

[33] K. Xu and G. Zha, "Design of high specific speed mixed flow micro-compressor for co-flow jet actuators." GT2019-90980, IGTI Turbo Expo 2019, Phoenix, Arizona, USA, DOI: 10.1115/GT2019-90980, June 17 - 21, 2019.

[34] Y. Wang and G. Zha, "Study of super-lift coefficient of co-flow jet airfoil and its power consumption," in *AIAA Aviation 2019 Forum*, pp. AIAA 2019–3652, 2019, DOI: 10.2514/6.2019-3652.

[35] Y. Wang and G. Zha, "Study of Mach number effect for 2d co-flow jet airfoil at cruise conditions," in *AIAA Aviation 2019 Forum*, pp. AIAA 2019–3169, 2019, DOI: 10.2514/6.2019-3169.

[36] M. L. Shur, P. R. Spalart, M. K. Strelets, and A. K. Travin, "A hybrid rans-les approach with delayed-des and wall-modelled les capabilities," *International Journal of Heat and Fluid Flow*, vol. 29, no. 6, pp. 1638–1649, 2008, DOI:10.1016/j.ijheatfluidflow.2008.07.001.

[37] Y. Yang and G. Zha, "Simulation of airfoil stall flows using IDDES with high order schemes." AIAA Paper 2016-3185, 46th AIAA Fluid Dynamics Conference,Washington, D.C., 13 June 2016, DOI: 10.2514/6.2016-3185.

[38] Y. Yang and G. Zha, "Improved delayed detached eddy simulation of super-lift coefficient of subsonic co-flow jet flow control airfoil." AIAA Paper 2018-0314, 2018 AIAA Aerospace Sciences Meeting, Kissimmee, Florida, 8-12 January 2018, DOI: 10.2514/6.2018-0314.

[39] B. Wang and G.-C. Zha, "Detached-eddy simulation of a coflow jet airfoil at high angle of attack," *Journal of aircraft*, vol. 48, no. 5, pp. 1495–1502, 2011, DOI: 10.2514/1.C000282.

[40] Y.-Q. Shen, G.-C. Zha, and B.-Y. Wang, "Improvement of Stability and Accuracy of Implicit WENO Scheme ," *AIAA Journal*, vol. 47, pp. 331–344, 2009.

[41] Shen, Y.-Q. and Zha, G.-C. and Chen, X.-Y., " High Order Conservative Differencing for Viscous Terms and the Application to Vortex-Induced Vibration Flows," *Journal of Computational Physics*, vol. 228(2), pp. 8283–8300, DOI:10.1016/j.jcp.2009.08.004, 2009.

[42] Shen, Y.-Q. and Zha, G.-C. , " Improvement of the WENO Scheme Smoothness Estimator," *International Journal for Numerical Methods in Fluids*, vol. DOI:10.1002/fld.2186, 2009.

[43] G.-C. Zha and E. Bilgen, "Numerical study of three-dimensional flows using unfactored upwind-relaxation sweeping algorithm," *Journal of Computational Physics*, vol. 125, no. 2, pp. 425–433, 1996, DOI: 10.1006/jcph.1996.0104.

[44] B. Wang, Z. Hu, and G.-C. Zha, "General subdomain boundary mapping procedure for structured grid implicit CFD parallel computation," *Journal of Aerospace Computing, Information, and Communication*, vol. 5, no. 11, pp. 425–447, 2008, DOI: 10.2514/1.35498.

[45] J. Gan, Y. Shen, and G. Zha, "Comparison of drag prediction using rans models and ddes for the dlr-f6 configuration using high order schemes," in *54th AIAA Aerospace Sciences Meeting*, p. 0553, AIAA 2016-0553, 2016, DOI: 10.2514/6.2016-0553.

[46] Y. Yang and G. Zha, "Numerical investigation of performance improvement of the co-flow jet electric airplane," in *AIAA Paper-2018-4208, AIAA AVIATION Forum, AIAA 2018-4208*, vol. 2018, pp. 25–29, 2018, DOI: 10.2514/6.2018-4208.

[47] H. Im, X. Chen, and G. Zha, "Simulation of 3d multistage axial compressor using a fully conservative sliding boundary condition," in *ASME 2011 International Mechanical Engineering Congress and Exposition*, pp. 1321–1330, American Society of Mechanical Engineers Digital Collection, 2011, DOI:10.1115/IMECE2011-62049.

[48] D. Espinal, H.-S. Im, and G.-C. Zha, "Full-annulus simulation of nonsynchronous blade vibration excitation of an axial compressor," *Journal of Turbomachinery*, vol. 140, no. 3, 2018, DOI: 10.1115/1.4038337.

[49] H. Im and G. Zha, "Investigation of flow instability mechanism causing compressor rotor-blade non-synchronous vibration," *AIAA Journal*, vol. 52, no. 9, pp. 2019–2031, 2014, DOI: 10.2514/1.J052781.

[50] H.-S. Im and G.-C. Zha, "Simulation of non-synchronous blade vibration of an axial compressor using a fully coupled fluid/structure interaction," in *ASME Turbo Expo 2012: Turbine Technical Conference and Exposition, GT2012-68150*, pp. 1395–1407, American Society of Mechanical Engineers Digital Collection, 2012, DOI: 10.1115/GT2012-68150.

[51] J. Gan, H.-s. Im, D. Espinal, A. Lefebvre, and G.-C. Zha, "Investigation of a compressor rotor non-synchronous vibration with and without fluid-structure interaction," in *ASME Turbo Expo 2014: Turbine Technical Conference and Exposition*, American Society of Mechanical Engineers Digital Collection, 2014, DOI: 10.1115/GT2014-26478.

[52] X.-Y. Chen and G.-C. Zha, "Fully coupled fluid-structural interactions using an efficient high resolution upwind scheme," *Journal of Fluids and Structures*, vol. 20, no. 8, pp. 1105–1125, 2005, DOI: 10.1016/j.jfluidstructs.2005.02.011.

[53] X. Chen, G.-C. Zha, and M.-T. Yang, "Numerical simulation of 3-d wing flutter with fully coupled fluid–structural interaction," *Computers & fluids*, vol. 36, no. 5, pp. 856–867, 2007, DOI: 10.1016/j.compfluid.2006.08.005.

[54] J.-y. Gan, H.-S. Im, X.-y. Chen, G.-C. Zha, and C. L. Pasiliao, "Delayed detached eddy simulation of wing flutter boundary using high order schemes," *Journal of Fluids and Structures*, vol. 71, pp. 199–216, 2017, DOI: 10.1016/j.jfluidstructs.2017.03.002.

[55] X. Chen, H. Im, and G.-C. Zha, "Fully coupled fluid-structural interaction of a transonic rotor at near-stall conditions using detached eddy simulation," in *49th AIAA Aerospace Sciences Meeting including the New Horizons Forum and Aerospace Exposition*, p. 228, 2011, DOI: 10.2514/6.2011-228.

[56] X. Chen and G. Zha, "Fully coupled fluid-structural interaction in a hybrid cartesian-body fitted grid system," in *40th Fluid Dynamics Conference and Exhibit*, p. 4611, AIAA 2010-4611, DOI: 10.2514/6.2010-4611.

[57] X. Chen and G. Zha, "Detached eddy simulation of 3-d wing flutter with fully coupled fluid-structural interaction," in *48th AIAA Aerospace Sciences Meeting Including the New Horizons Forum and Aerospace Exposition*, p. 53, AIAA 2010-53,2010, DOI:10.2514/6.2010-53.

[58] Y. Yang and G. Zha, "Super-lift coefficient of active flow control airfoil: What is the limit?." AIAA Paper 2017-1693, AIAA SCITECH2017, 55th AIAA Aerospace Science Meeting, Grapevine, January 9-13 2017, DOI: 10.2514/6.2017-1693.

[59] Im, H.-S. and Zha, G.-C. and Dano, B. P. E., "Large Eddy Simulation of Coflow Jet Airfoil at High Angle of Attack," *Journal of Fluid Engineering, vol. 136(2), p. 021101*, 2014, DOI: 10.1115/1.4025649.

[60] H.-S. Im and G.-C. Zha, "Delayed detached eddy simulation of airfoil stall flows using high-order schemes," *Journal of Fluids Engineering*, vol. 136, no. 11, 2014, DOI: 10.1115/1.4027813.

[61] V. N. Vatsa, D. Casalino, J. C. Lin, and J. Appelbaum, "Numerical simulation of a high-lift configuration with embedded fluidic actuators." AIAA Paper 2014-2142, 32nd AIAA Applied Aerodynamics Conference, Atlanta, GA, 16-20 June 2014, DOI: 10.2514/6.2014-2142.